PNAS RESEARCH ARTICLE | GENETICS

An E2 ubiquitin-conjugating enzyme links diubiquitinated H2B to H3K27M oncohistone function

Alan L. Jiao[a,b,1], Erdem Sendinc[b,2,3], Barry M. Zee[b,4], Felice Wallner[a,b], and Yang Shi[a,b,1]

Affiliations are included on p. 9.

Contributed by Yang Shi; received August 19, 2024; accepted October 17, 2024; reviewed by Chao Lu and Capucine Van Rechem

The H3K27M oncogenic histone (oncohistone) mutation drives ~80% of incurable childhood brain tumors known as diffuse midline gliomas (DMGs). The major molecular feature of H3K27M mutant DMGs is a global loss of H3K27 trimethylation (H3K27me3), a phenotype conserved in *Caenorhabditis elegans* (*C. elegans*). Here, we perform unbiased genome-wide suppressor screens in *C. elegans* expressing H3K27M and isolate 20 suppressors, all of which at least partially restore H3K27me3. 19/20 suppressor mutations map to the same histone H3.3 gene in which the K27M mutation was originally introduced. Most of these create single amino acid substitutions between residues R26-Y54, which do not disrupt oncohistone expression. Rather, they are predicted to impair interactions with the Polycomb Repressive Complex 2 (PRC2) and are functionally conserved in human cells. Further, we mapped a single extragenic H3K27M suppressor to *ubc-20*, an E2 ubiquitin-conjugating enzyme, whose loss rescued H3K27me3 to nearly 50% wild-type levels despite continued oncohistone expression and chromatin incorporation. We demonstrate that *ubc-20* is the major enzyme responsible for generating diubiquitinated histone H2B. Our study provides in vivo support for existing models of PRC2 inhibition via direct oncohistone contact and suggests that the effects of H3K27M may be modulated by H2B ubiquitination.

Oncohistone | H3K27M | diffuse midline glioma | *C. elegans* | epigenetics

Significance

Approximately ~80% of incurable childhood brain tumors known as diffuse midline gliomas (DMGs) are driven by the H3K27M histone mutation. How H3K27M causes tumors is not fully understood. One approach to better understand the molecular functions of H3K27M is to identify mutations that detoxify, or suppress, its effects. Facilitating this approach, histones and their functions are highly conserved throughout animal species, including *Caenorhabditis elegans*. Here, using genome-wide screens in *C. elegans*, we isolate 20 mutations which suppress H3K27M phenotypes. Nineteen of these mapped to the K27M mutant histone itself. A single mutation mapped to *ubc-20*, an E2 ubiquitin-conjugating enzyme, which we show is required for diubiquitination of histone H2B. Our data suggest differentially ubiquitinated nucleosomes may regulate oncohistone function.

Approximately ~80% of incurable pediatric brain tumors known as diffuse midline gliomas (DMGs) are driven by the K27M mutation in histone H3 (1–5). Despite consisting of a small fraction of the total histone H3 pool, K27M oncogenic histones (oncohistones) dramatically reshape the H3K27 methylation landscape (6–10). H3K27 mono-, di-, and trimethylation (H3K27me1/2/3) are catalyzed by the Polycomb Repressive Complex 2 (PRC2) (11). K27M dominantly inhibits PRC2, leading to a widespread reduction of H3K27me2/3, with residual H3K27me3 enriched as narrow peaks at or near strong sites of PRC2 recruitment (9, 12, 13). This epigenetic dysregulation is thought to be a major contributor to K27M oncogenic potential. H3K27me3 is associated with repressive chromatin and maintains the silencing of cell type–specific genes, serving as a crucial regulator of cell identity and cell fate decisions (14, 15). K27M-dependent inhibition of PRC2 activity impairs the differentiation capacity of glial progenitor cells and is thought to promote a proliferative, stem-like cell state that drives tumorigenesis (16–20).

Numerous studies have investigated the molecular mechanisms underlying how K27M inhibits PRC2. H3K27M peptides were found to exhibit significantly greater binding affinities to PRC2 compared to wild-type H3 peptides, and thus, act as competitive inhibitors for substrate binding (9, 21). A sequestration model was proposed, where a limited pool of PRC2 would be sequestered by K27M oncohistones away from wild-type histones (9, 21). However, five observations potentially complicate this model. First, PRC2–oncohistone interactions were not consistently detected in coimmunoprecipitation experiments (6, 12, 22–24). Second, unlike H3K27M mutant peptides, H3K27M mutant nucleosomes did not exhibit significantly greater binding affinities to PRC2 (25); instead PRC2-nucleosome affinities were primarily dictated by interactions with DNA (25–27). Third, H3K27M was found to be excluded from PRC2 targets (28). Fourth, K27M oncohistones and an oncohistone-like protein (EZHIP) do not require incorporation into chromatin for their PRC2-inhibitory effects (12, 29). Fifth, K27M may impart a lasting inhibitory effect on PRC2 activity (even after K27M removal), potentially through regulation of PRC2 automethylation (30, 31).

While the molecular details of K27M-dependent epigenetic dysregulation remain to be fully elucidated, attempts to exploit oncohistone-specific vulnerabilities through epigenetically targeted therapies have shown preclinical promise (13, 28, 32–35). Other studies have explored ways to detoxify (i.e., suppress) K27M effects, both in vitro

[1]To whom correspondence may be addressed. Email: alan.jiao@ludwig.ox.ac.uk or yang.shi@ludwig.ox.ac.uk.

[2]Present Address: Stem Cell Program, Division of Hematology/Oncology, Boston Children's Hospital, Boston, MA 02115.

[3]Present Address: Department of Biological Chemistry and Molecular Pharmacology, Harvard Medical School, Boston, MA 02115.

[4]Present Address: Cell Signaling Technology Inc., Danvers, MA 01923.

This article contains supporting information online at https://www.pnas.org/lookup/suppl/doi:10.1073/pnas.2416614121/-/DCSupplemental.

Published November 19, 2024.

(36) and in vivo, in model organisms such as *Drosophila melanogaster* (37) and *Caenorhabditis elegans* (38). These studies have shed light on oncohistone-dependent mechanisms but have generally been limited in scale: To our knowledge, a genome-wide screen for K27M suppressors has not been carried out to saturation. As a result, mutants which restore PRC2 activity in a K27M background have not been identified in an unbiased or exhaustive manner.

Here, we performed saturating genome-wide suppressor screens in *C. elegans* and isolated 20 independent K27M suppressor mutations, nearly all of which restore H3K27me3. Nineteen of these mapped to the K27M-mutant histone itself, while one mutation mapped to *ubc-20*, an E2 ubiquitin-conjugating enzyme. We identify diubiquitinated H2B as the catalytic product of *UBC-20*. Our data provide in vivo support for existing models of PRC2 inhibition via direct oncohistone contact and suggest that the effects of H3K27M can be modulated by H2B ubiquitination.

Results

A Genome-Wide Screen for K27M Suppressors. To establish a screening platform for identifying mutants that rescue H3K27M phenotypes, we first introduced the K27M mutation into the endogenous H3.3 gene (*his-72*) in *C. elegans* (hereafter referred to as "K27M mutants") (*SI Appendix*, Fig. S1*A*). Similar to previous reports in K27M-mutant DMGs (9), mass spectrometry indicated the oncohistone consisted of only ~5% of the total H3 pool (*SI Appendix*, Fig. S1*B* and Table S1) but caused a dramatic global loss of H3K27me3 and H3K27me2 (*SI Appendix*, Fig. S1*C*). Thus, key molecular features of K27M-mutant human gliomas are recapitulated in *C. elegans*.

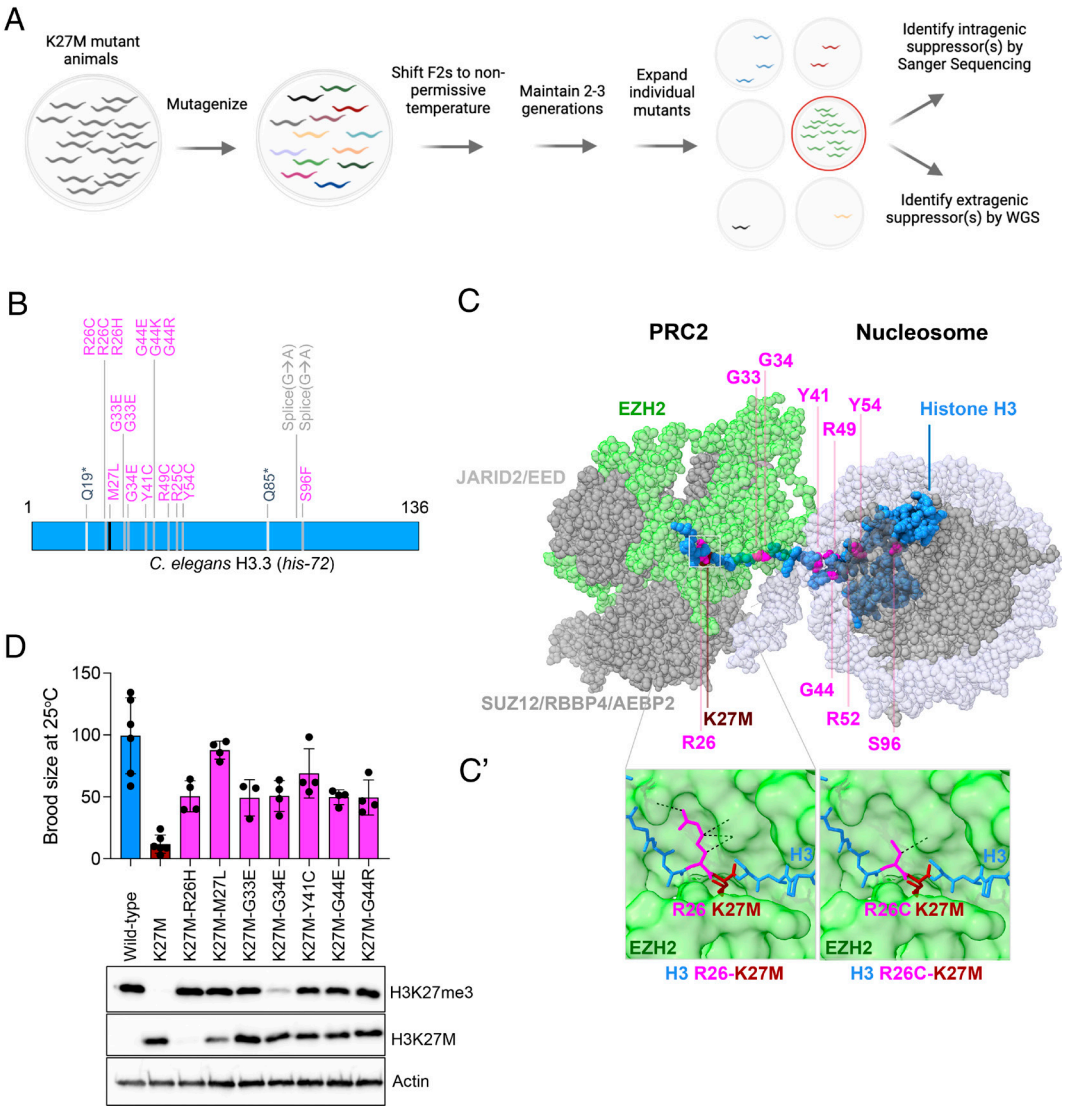

Fig. 1. Genome-wide H3K27M suppressor screen identifies H3.3 residues required for oncohistone function. (*A*) Schematic of genome-wide mutagenesis screen for K27M suppressors. K27M mutants were expanded at the permissive temperature (20 °C) and then mutagenized with either EMS or ENU as L4s. F2 offspring were shifted to the nonpermissive temperature at 25 °C as larvae and maintained for 2 to 4 generations before individual animals were isolated onto individual plates. Candidate suppressor strains were selected based on high fertility at 25 °C. (*B*) Position and identity of the 19 intragenic suppressors in H3.3 (HIS-72) identified by Sanger sequencing. * indicates nonsense mutation. (*C*) Cryo-EM structure of human PRC2 bound to a nucleosome (PDB: 6 wk) (40). Positions of K27M suppressor mutations are colored magenta and mapped onto the H3 peptide substrate (blue). (*C'*) Surface representation of the substrate binding site in the EZH2 SET domain containing an H3 peptide substrate (blue), shown in stick representation. Black dashed lines indicate contacts between the side chain of residue 26 in histone H3 and EZH2 predicted by structure analysis in ChimeraX. Upper panel shows unmutated R26; bottom panel shows the R26C suppressor mutation, which abolishes key contacts with EZH2. (*D*) Suppressor phenotypes as measured by brood sizes at the nonpermissive temperature (25 °C) and by Western blotting for H3K27me3. Error bars represent SD. Each dot represents the average brood size of three individual animals. All mutants were backcrossed at least four times. Protein lysates were collected from overnight-starved populations of adults and L1 larvae.

K27M mutant animals were fertile at optimal growth temperatures (20 °C) but, unlike wild-type animals, became sterile at higher (25 °C) temperatures (*SI Appendix*, Fig. S2). This conditional sterility is consistent with incomplete PRC2 inhibition by K27M, as PRC2 null mutants in *C. elegans* give rise to progeny which are fully sterile (39). We hypothesized temperature-sensitive sterility could enable efficient suppressor screens: following mutagenesis, any K27M mutant animals that were still fertile after 2 to 4 generations at the nonpermissive temperature would be expected to carry additional mutation(s) that could suppress the effects of K27M (Fig. 1*A*). Using this approach, we screened ~200 million mutations over five independent screens. In total, we isolated 20 K27M suppressors.

Histone H3.3 N-Terminal Mutations Suppress K27M Phenotypes in *cis*. Hypothesizing that the most potent K27M suppressor mutations would be intragenic, we performed Sanger sequencing of the K27M-mutated H3.3 gene in all suppressor strains. Remarkably, 19/20 suppressor mutants carried intragenic H3.3 mutations, concentrated between residues R26-Y54 (Fig. 1 *B* and *C*). These results support the validity and saturation of the screen. Four mutations resulted in predicted null alleles, while all others created single amino acid substitutions. Notably, a K27M-M27L mutation restored fertility to wild-type levels (Fig. 1*D*). Although K27M-M27L mutant histones cannot undergo methylation at position 27, this mutation rescued the global H3K27me3 methylation level (Fig. 1*D*). This suggests that the fertility defect is not caused by the absence of K27 methylation on the mutant H3.3 histone, but rather by the inhibition of PRC2 activity, which affects global H3K27 methylation.

Three independent suppressors carried H3.3R26 mutations, which were previously shown to detoxify oncohistone effects in human cells (36). R26 mutations abrogate hydrogen bonding with EZH2 side chains that form a well-defined pocket in the histone H3 substrate binding site (Fig. 1*C'*), normally required for the specific recognition of the target lysine by PRC2 (21). Most other single amino acid substitutions were localized at or near the N-terminal H3 tail and were predicted to disrupt interactions with human PRC2 complex via altering interactions with DNA at the nucleosome entry/exit sites (Fig. 1*C*). These include R49 and R52 mutations, which have been shown to be required for H3K36 tri- (but not mono- or di-) methylation (41), as well as three independent G44 mutations. Importantly, most substitutions tested rescued both fertility and H3K27me3 levels without affecting oncohistone expression (Fig. 1*D*). An apparent exception was H3.3R26H-K27M, whose expression was not detected by the anti-K27M antibody (Fig. 1*D*). However, expression of a FLAG-tagged H3.3R26A-K27M could be detected by anti-FLAG in human cells (Fig. 2*B* below), suggesting that R26 mutant oncohistones are also expressed in *C. elegans* but just not recognized by anti-K27M.

Thus, despite evidence that H3.3K27M and PRC2/H3K27me3 generally do not colocalize on chromatin (10, 28, 38, 42), our data strongly suggest that direct physical contact is required for PRC2 inhibition by H3K27M in vivo. Taken together with the existing literature, our data can be reconciled by a model whereby H3K27M oncohistones, potentially via internucleosomal interactions and/or as soluble factors (12), directly bind to and inhibit PRC2 without sequestration.

H3.3K27M Suppressor Mutations are Functionally Conserved. We next tested the functional conservation of suppressor mutations in human cells. We used a lentiviral FLAG-HA-tagged H3.3 construct fused to GFP via an internal ribosome entry sequence, enabling GFP levels to control for infection efficiencies and FLAG levels to assess mutant histone expression (Fig. 2*A*). As expected, expression of K27M-mutant H3.3 potently reduced H3K27me3 (Fig. 2*B*). Importantly, most suppressor mutations identified in *C. elegans*, when cointroduced in *cis,* rescued H3K27me3 in human cells (Fig. 2*B*). We also tested the effects of additional K-to-M mutations (K4M, K9M, and K36M) on K27M function and found that both K4M and K36M could partially suppress K27M-mediated inhibition of H3K27me3 (Fig. 2*B*). We conclude that PRC2 inhibition by H3.3K27M oncohistones is most sensitive to the amino acid composition between R26 and Y54 of histone H3.3.

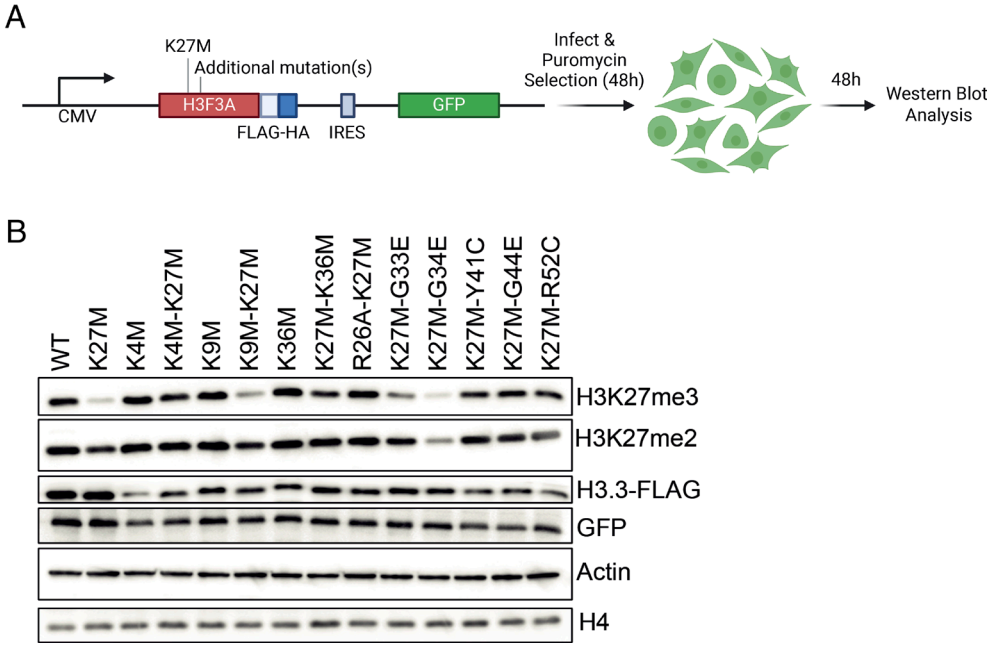

Fig. 2. Intragenic suppressors identified in *C. elegans* are functionally conserved in human cells. (*A*) Construct and experimental design for mutant histone expression. IRES, internal ribosome entry site. (*B*) Western blot demonstrating the effects of mutant histone expression on H3K27me2/3. HEK293T cell lysates were collected 96 h postinfection. Actin and histone H4 serve as loading controls, GFP expression serves to control for infection efficiencies.

Interestingly, G34E mutations were unique among *C. elegans* suppressors in rescuing K27M-induced sterility while only weakly rescuing H3K27me3 (Fig. 1*D*). G34E mutations cointroduced with K27M also did not restore H3K27me3 in human cells (Fig. 2*B*). These results suggest some K27M phenotypes can be at least partially uncoupled from H3K27me3. While H3 G33/34 may not directly interact with PRC2, it can act as a flexible hinge between H3 A29/P30 and H3 V35, two regions previously shown to interact with PRC2 (43). Suppression of H3K27M phenotypes by G34 mutations provides a potential mechanistic explanation for the mutual exclusivity of K27M and G34 histone mutations in human gliomas (44).

Loss of Function in *ubc-20* Suppresses K27M Phenotypes. To identify the single extragenic suppressor, we backcrossed the suppressor strain to unmutagenized K27M mutant animals and followed the suppressor mutation by Western blotting in expanded F2 clonal lines for rescued H3K27me3. Whole-genome sequencing identified the causal suppressor as a G155R mutation in *ubc-20*, a poorly characterized E2 ubiquitin-conjugating enzyme (Fig. 3*A*). K27M;*ubc-20* mutants exhibited partially restored fertility at the nonpermissive temperature (Fig. 3*B*). Rescue of H3K27me3 was most pronounced following an arrest in cell division (by overnight starvation of larvae), to limit the replicational dilution of histone methylation, which enabled K27M;*ubc-20* mutants (but not K27M mutants) to restore H3K27me3 to ~45% of wild-type levels (Fig. 3 *C* and *D*).

RNA interference (RNAi) against *ubc-20* also rescued H3K27me3 in K27M mutants (Fig. 3*E*), confirming that *ubc-20* was the causal suppressor and that *ubc-20*(G155R) was a loss of function mutation. H3K27me3 levels in a H3.3 wild-type background were largely unaffected by *ubc-20* RNAi (Fig. 3*F*) and by *ubc-20*(G155R) (Fig. 3*G*), suggesting a K27M-specific effect of *ubc-20* on H3K27me3. Restoration of H3K27me3 in *ubc-20* mutants remained dependent on the *C. elegans* core PRC2 subunit *MES-3* [a divergent

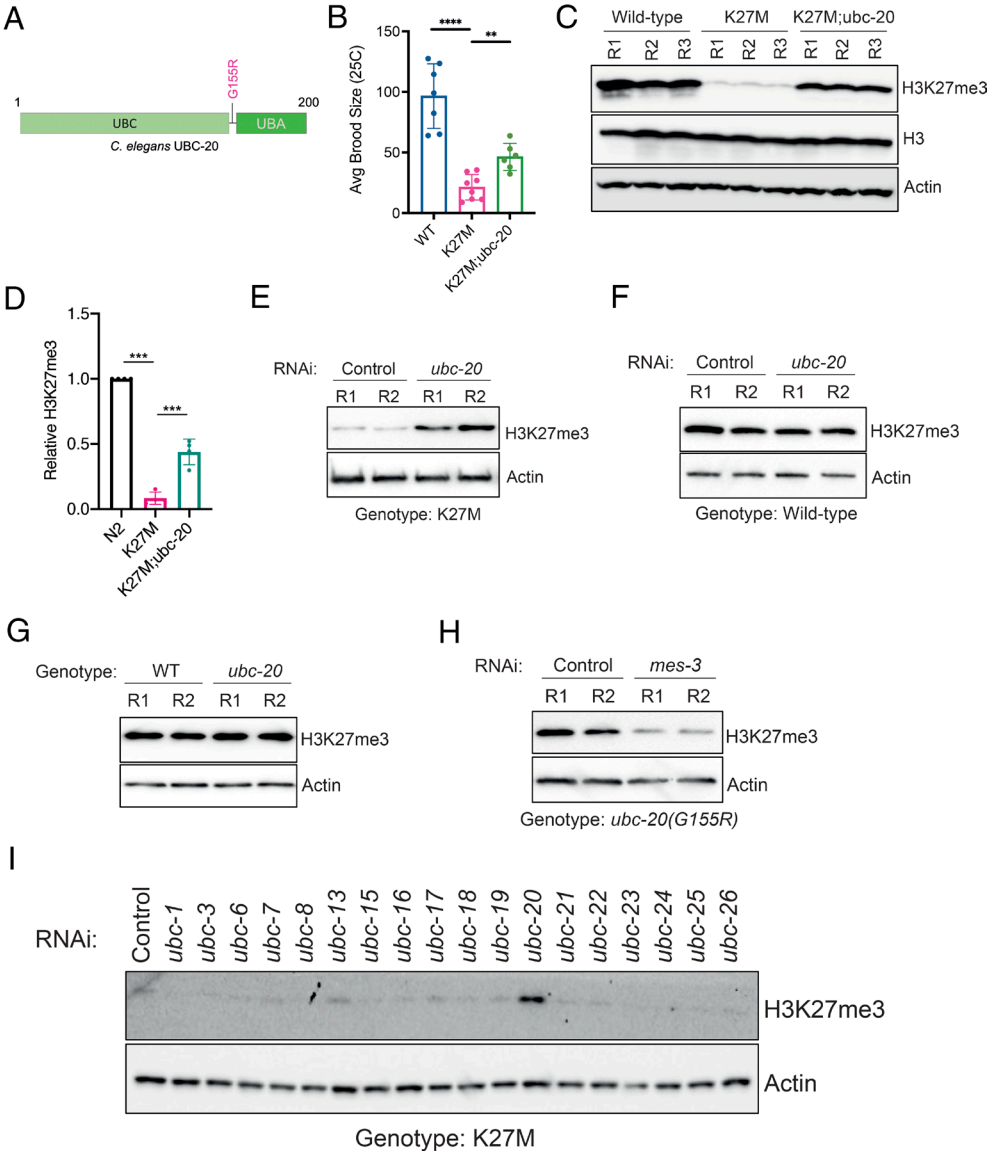

Fig. 3. Loss of *ubc-20* rescues H3K27me3 levels in K27M mutants. (*A*) Schematic of *C. elegans* UBC-20. The G155R mutant allele identified from the K27M suppressor screen is indicated. (*B*) Mean fertility of the indicated genotypes at 25 °C. Error bars represent SD. Each dot represents the average brood size of three individual animals. ****$P < 0.0001$; **$P < 0.005$, two-tailed *t* test. (*C*) Western blots of *C. elegans* lysates collected from L2 larvae grown on NA22-seeded plates and starved overnight. The K27M;*ubc-20* suppressor was backcrossed five times. R, biological replicate. (*D*) Quantification of H3K27me3 Western blot signal normalized to Actin shown in (*C*). (*E* and *F*) Western blot of L2 larvae lysates collected from K27M (*E*) or wild-type (*F*) animals following *ubc-20* RNAi. (*G*) Western blots of L2 larvae lysates collected from wild-type and *ubc-20*(G155R) mutants. (*H*) Western blots of L2 larvae lysates collected from *ubc-20*(G155R) mutants following *mes-3* RNAi. (*I*) Western blots of L2 larvae lysates collected from K27M mutants following RNAi of the indicated E2 ubiquitin-conjugating enzymes.

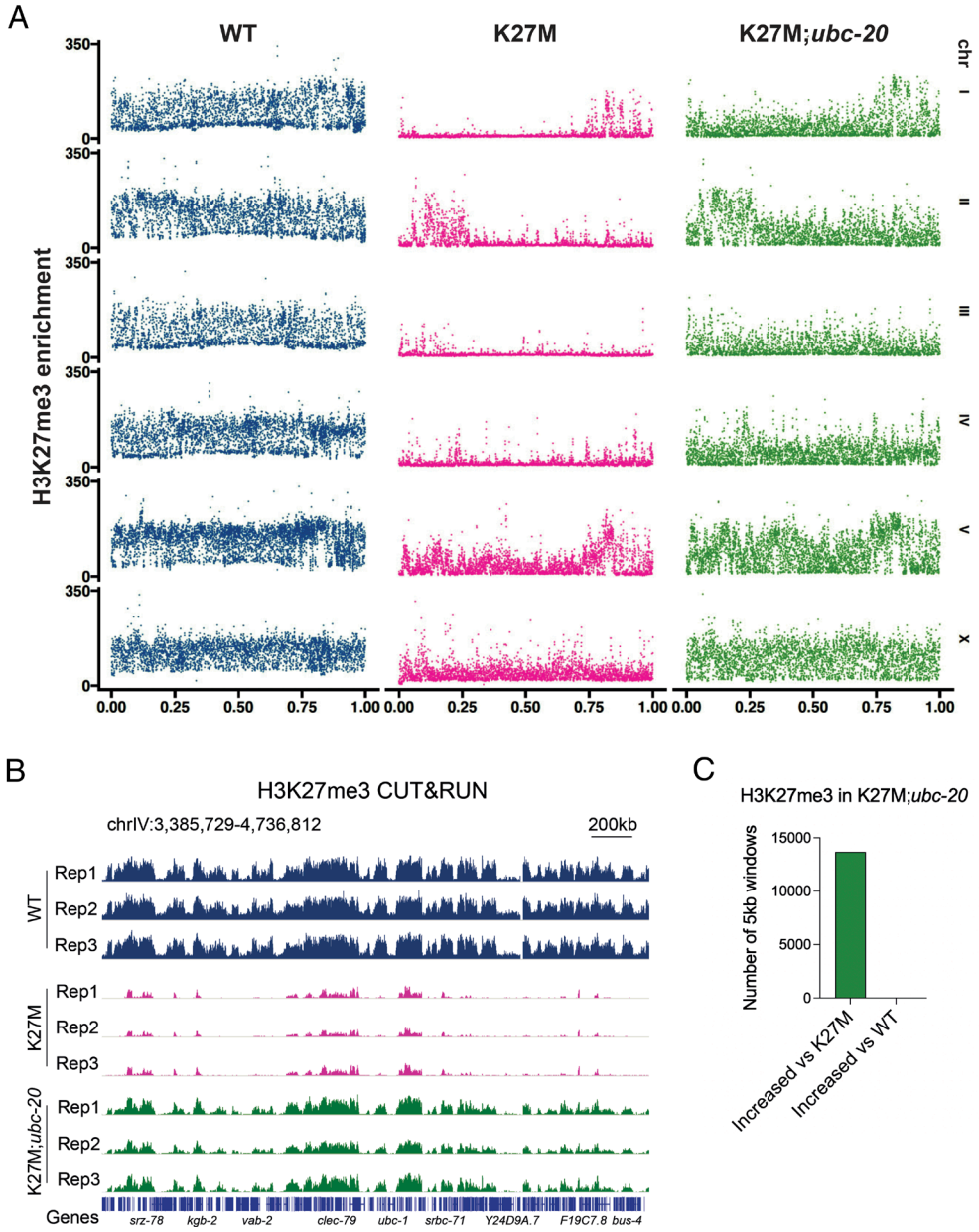

Fig. 4. Loss of *ubc-20* correctly restores endogenous H3K27me3 patterns in K27M mutants. (*A*) Distribution of spike-in-normalized H3K27me3 CUT&RUN signal along each chromosome in wild-type and mutant L2 larvae. Each dot represents the average H3K27me3 signal in a 5 kb window (n = 3 independent replicates). All chromosomes were normalized to the same length. (*B*) Representative IGV tracks of spike-in-normalized H3K27me3 CUT&RUN. (*C*) Number of 5 kb genomic regions in K27M;*ubc-20* mutants with differential H3K27me3 CUT&RUN enrichment (>2-fold) compared to K27M or wild-type animals.

ortholog of human SUZ12 (45)] (Fig. 3*H*), arguing against gain-of-function mechanisms by other histone methyltransferases.

The *C. elegans* genome contains 20 E2 ubiquitin-conjugating enzymes (46). Because E2 ubiquitin-conjugating enzymes can exhibit functional redundancies, we tested whether targeting E2s other than *ubc-20* can also suppress K27M phenotypes. We individually depleted the 18 nonessential E2s by RNAi, but notably, *ubc-20* was the only E2 enzyme whose depletion rescued H3K27me3 (Fig. 3*I*).

Loss of *ubc-20* Restores Wild-Type Patterns of H3K27me3. To test whether H3K27me3 in K27M mutants was being restored in the correct genomic regions upon loss of *ubc-20,* we performed spike-in-normalized CUT&RUN for H3K27me3 in wild-type, K27M, and K27M;*ubc-20* mutants. To generate a global view of the H3K27me3 landscape for each genotype, we plotted the average H3K27me3 CUT&RUN signal in each 5 kb window along each of the six *C. elegans* chromosomes (Fig. 4*A*). As in K27M-mutant gliomas, H3K27me3 was not uniformly lost in K27M mutant animals but was preferentially retained at certain strong PRC2 targets including the X chromosome (47) (Fig. 4*A*). Remarkably, K27M;*ubc-20* mutants exhibited rescued H3K27me3 across the genome, without accumulation beyond wild-type levels or at ectopic sites (Fig. 4 *A* and *B*); of 13,681 5 kb genomic windows which showed increased (>2-fold) H3K27me3 in H3.3K27M;*ubc-20* vs. K27M, none were increased (>2-fold) vs. wild-type. (Fig. 4*C*). These data indicate that loss of *ubc-20* correctly restores the endogenous distribution of H3K27me3 in K27M mutants.

UBC-20 Does Not Target MES-2 or K27M for Degradation. We postulated that increased levels of PRC2 proteins, and/or reduced levels of H3.3K27M oncohistones, were two potential

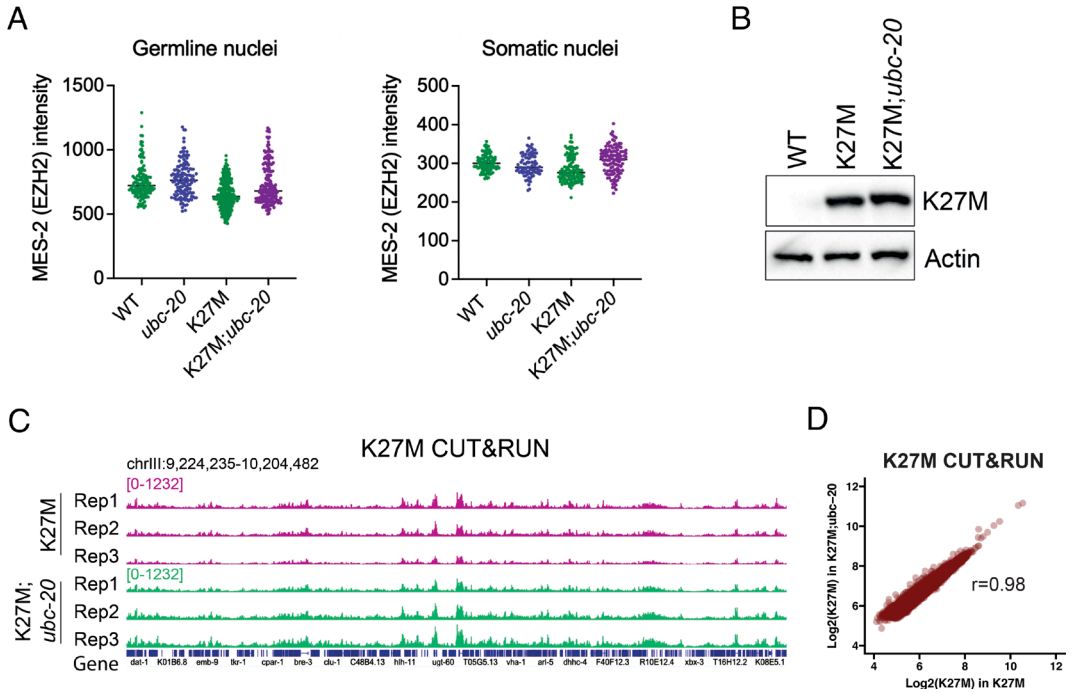

Fig. 5. H3K27me3 rescue in K27M;*ubc-20* mutants is not associated with altered MES-2 or H3K27M expression. (*A*) MES-2::GFP intensities measured in adult germline nuclei and L2 larvae pharyngeal nuclei. Each dot represents the GFP intensity in a single nucleus. GFP in at least 100 nuclei from at least 10 animals were quantified per genotype. (*B*) Western blot of K27M oncohistone expression in mixed-stage animals. (*C*) Representative IGV tracks of spike-in-normalized H3K27M CUT&RUN of L2 larvae. (*D*) Scatter plot of spike-in-normalized H3K27M CUT&RUN signal in K27M;*ubc-20* vs. K27M L2 larvae. Each dot represents the average H3K27M signal in a 5 kb window (n = 3 independent replicates). The Pearson correlation coefficient is indicated.

mechanisms through which loss of *ubc-20* may rescue H3.3K27M phenotypes. However, MES-2 [the *C. elegans* catalytic PRC2 subunit and homolog of human EZH2 (47)] protein levels were minimally affected in the germline and in somatic cells in *ubc-20* mutants (Fig. 5*A*), arguing against a rescue mechanism via increased PRC2 expression. Similarly, H3.3K27M oncohistone expression (Fig. 5*B*) and incorporation into chromatin (Fig. 5 *C* and *D*) were minimally affected by *ubc-20*. Thus, loss of *ubc-20* relieves oncohistone-dependent H3K27me3 inhibition without altering H3.3K27M expression or chromatin distribution.

UBC-20 Catalyzes H2B Diubiquitination. We next tested whether *ubc-20* might ubiquitinate histones. Monoubiquitination of histone H2A and H2B (on K120 and K116, respectively, in *C. elegans*) are abundant, highly conserved modifications in eukaryotes known to regulate H3 methylation (48–51). H2A and H2B monoubiquitination were unaffected in *ubc-20* mutants (Fig. 6*A*). However, while probing for monoubiquitination, we also observed a larger protein species whose size corresponded to the diubiquitinated form of each histone. Importantly, putatively diubiquitinated H2B (H2Bub2) was uniquely abolished in *ubc-20* mutants (Fig. 6*A*). This is consistent with *ubc-20* homologs extending polyubiquitin chains with K48 linkage specificity (52–54) and with polyubiquitinated H2B being primarily characterized by K48 linkages (55). Putative H2Bub2 was sensitive to H2Bub1 depletion (*SI Appendix*, Fig. S3*A*) and was also eliminated by introducing a C92S mutation in the conserved catalytic cysteine of endogenous *ubc-20* (Fig. 6*B*). Our data suggest that diubiquitinated H2B, an uncharacterized histone modification, is generated by UBC-20-dependent ubiquitination of a previously monoubiquitinated H2B substrate.

To further investigate *ubc-20*-dependent ubiquitination, we tagged the endogenous *ubc-20* locus with an N-terminal 3XFLAG. While the fusion protein was successfully expressed in a K27M mutant background (*SI Appendix*, Fig. S3*B*), it was nonfunctional, as evidenced both by the loss of H2Bub2 and the concomitant rescue of H3K27me3 (Fig. 6*B*). These data suggest the endogenous N terminus of UBC-20 is required for ubiquitin-conjugating activity and is consistent with the first nine amino acids of *RAD6/UBC2*, another highly conserved E2 enzyme, being required for catalytic activity (49). H2Bub2 levels were not significantly affected by proteasome inhibitor treatment (Fig. 6*C*), supporting the notion that, like monoubiquitination, diubiquitination of H2B does not direct proteasome-mediated degradation but instead may regulate cross-talk between other histone modifications.

To assess whether the *ubc-20* phenotype could be phenocopied by depleting *rfp-1*, the E3 enzyme directly required for H2Bub1 (56) (and indirectly required for H2Bub2), we treated K27M mutants with *rfp-1* RNAi. Consistent with *rfp-1* not being a hit from our suppressor screen, *rfp-1* depletion did not restore H3K27me3 (*SI Appendix*, Fig. S3*C*). These data suggest loss of H2Bub2 is insufficient to relieve PRC2 inhibition; rather, H3K27M function remains sensitive to the relative abundance of H2Bub1/ub0. Considering most, if not all, other H3K27M suppressors identified in our screen are predicted to disrupt oncohistone–PRC2 interactions, we propose K27M-mutant nucleosomes containing H2Bub2 or H2Bub0 interact with and inhibit PRC2 more potently than those containing H2Bub1 (Fig. 6*D*). Thus, loss of *ubc-20* selectively depletes a state of K27M-mutant nucleosomes capable of PRC2 inhibition.

Discussion

Here, we performed saturating genome-wide screens for K27M suppressors. We isolated 20 independent suppressor mutations, most of which were concentrated between residues R26-Y54 of the K27M-mutated H3.3 gene. EZH2 forms an extensive network of interactions between the nucleosomal DNA and the H3 N

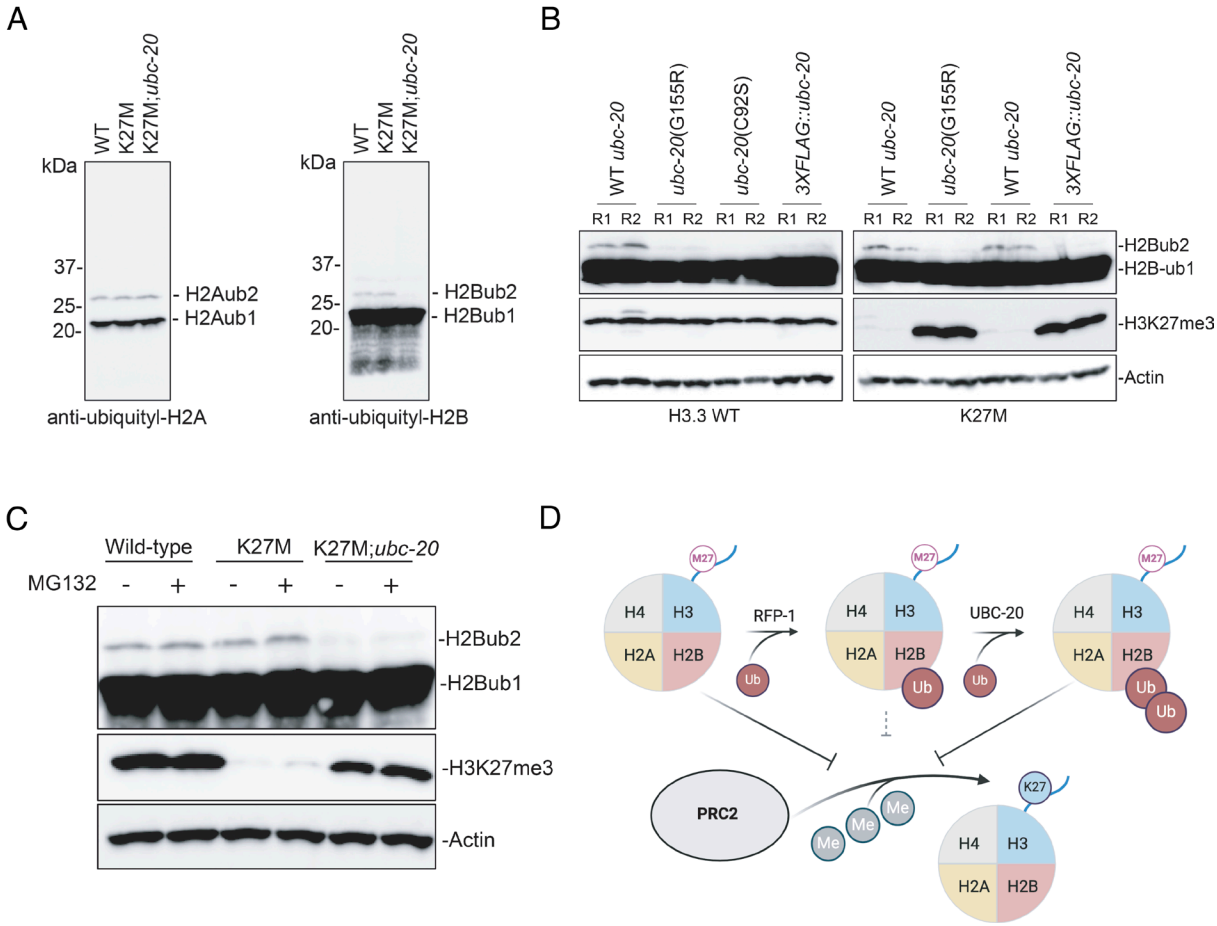

Fig. 6. UBC-20 enzymatic activity is required for H2B diubiquitination. (*A*–*C*) Western blots of lysates from starved L2 larvae. In (*C*), larvae were exposed to 80 μM of MG132 proteasome inhibitor in M9 buffer for 20 h. R, replicate. (*D*) Model of *ubc-20*-dependent H2B diubiquitination and regulation of K27M-mediated PRC2 inhibition. UBC-20 acts on monoubiquitinated H2B substrates to generate diubiquitinated histone H2B. K27M mutant nucleosomes containing diubiquitinated H2B, but not monoubiquitinated H2B, potently inhibit PRC2.

terminus (43), involving histone residues that display a remarkable overlap with those that, when mutated, detoxify K27M phenotypes. Thus, our data strongly suggest that direct oncohistone–PRC2 contacts are required for PRC2 inhibition, independently of the relative importance of PRC2 sequestration (6, 8, 10, 28). We favor a model in which the H3K27M–PRC2 interaction is sufficient to outcompete wild-type histone H3 tails for the PRC2 active site, but insufficient to redirect PRC2 localization, which is predominantly dictated by other chromatin features (57).

Because the suppressor screen was performed to saturation, mutations which were *not* identified as suppressors are themselves informative. For example, consistent with previous work suggesting H3K27M can function without chromatin deposition, mutations that affect incorporation of H3 into chromatin, such as H3I126A and H3L130A required for H3-H4 tetramer formation, were not isolated (12). Moreover, specific mutations in PRC2 or H3K36 methyltransferase complexes might have been expected to act as K27M suppressors but were also not isolated. Our findings point to *ubc-20* as one of the only non-H3.3 genes that may be targetable for suppressing K27M phenotypes.

We identified a potential role for *ubc-20*-dependent H2B diubiquitination in regulating PRC2 activity, but only in the context of K27M-expressing cells—suggesting that H2Bub2 affects oncohistone function rather than directly regulating PRC2. It is unlikely that K27M-mutant nucleosomes decorated with different chemical modifications all inhibit PRC2 with equal potency. Just as how H2Bub1 stabilizes the active conformations of nucleosome-bound COMPASS (58, 59) and DOT1L (60) histone methyltransferases, our data suggests that H2Bub2 may stabilize PRC2 bound to H3K27M-mutant nucleosomes. As each ubiquitin molecule (~8 kDa) is about half the size of a histone, nucleosomes containing un-, mono-, or diubiquitinated H2B exhibit unique structural features, which could either promote or prevent oncohistone–PRC2 interactions. Because simultaneous depletion of H2Bub2 and H2Bub1 did not suppress K27M phenotypes, we propose a model where K27M-mutant nucleosomes containing either H2Bub2 or H2Bub0, but not H2Bub1, are the major nucleosomal states that drive PRC2 inhibition (Fig. 6*D*). This model is consistent with the enrichment of H2Bub1 at actively transcribed loci (61), which are marked with H3 modifications (e.g., H3K4me3 and H3K36me2/3) known to antagonize interactions with PRC2 (49, 62, 63).

It is important to note that we have not ruled out UBC-20-dependent ubiquitination of nonhistone targets as the relevant mechanism of K27M suppression. However, it is well established that histone methyltransferase activity is sensitive to histone ubiquitination. In human cells, monoubiquitinated H2AK119 promotes PRC2 activity (50), while monoubiquitinated H2BK120 is required for H3K4 and H3K79 methylation (48, 49, 51, 64). Given our findings, it will be important to determine the structures and relative activity of PRC2 with un-, mono-, and di-ubiquitinated H2B nucleosomes with H3K27M. H2B di-ubiquitination has also been detected in human cells (65), but its cognate enzyme and biological function are not known. The closest mammalian homolog to *ubc-20*

is *UBE2K*, which has been reported to extend K48-linked polyubiquitin chains to induce substrate degradation (53, 54). Despite being predominantly localized to the cytoplasm, UBE2K has been shown to ubiquitinate histone H3 and regulate neuronal differentiation (66). Whether UBE2K mediates H2B di-ubiquitination and can be targeted to suppress K27M phenotypes in human cells remains an exciting area of future investigation.

Materials and Methods

***C. elegans* Strain Maintenance.** *C. elegans* were maintained on NGM plates seeded with OP50 at 20 °C unless otherwise noted. The wild-type strain used was Bristol N2. Some strains were provided by the CGC, which is funded by NIH Office of Research Infrastructure Programs (P40 OD010440). Some strains were generated by SunyBiotech. All strains used and generated are listed in *SI Appendix*, Table S2.

***C. elegans* Strain Generation by CRISPR-Cas9.** To generate H3.3K27M mutants, a co-conversion strategy was used (67) to mutate the endogenous *his-72* gene. N2 adults were injected with 25 ng/μL of Cas9 plasmid (Addgene 46168), 15 ng/μL of dpy10 gRNA, 40 ng/μL of his-72 gRNA, 200 ng/μL of each ssODN repair template, and 0.5 μL of 1 kb DNA ladder per 10 μL of injection mix. gRNAs were injected as PCR products amplified from gRNAs cloned into Addgene 46169. The endogenous 3xFLAG::*ubc-20* and *ubc-20*(C92S) mutant strains were generated by SunyBiotech.

Suppressor Screen. Thousands of K27M mutant L4 animals were mutagenized in either 47 mM ethyl methanesulfonate (EMS, four independent screen replicates) or 0.6mM N-ethyl-N-nitrosourea (ENU, one screen replicate) for 4 h rocking at room temperature. Animals were washed three times in M9 and recovered at 20 °C on NGM plates seeded with either op50 or NA22 *E. coli*. F1 adults were bleached to obtain synchronized F2 embryos, which were transferred to 25 °C as early larvae. Subsequent generations (F3–F6) were isolated either by washing off parental adults once many embryos have been laid or by bleaching. Once the majority of the population became sterile (after 2 to 4 generations at 25 °C), hundreds of individual candidate suppressors were picked onto individual op50 plates and allowed to recover at 20 °C. Progeny of fertile isolates were retested for fertility at 25 °C to confirm their phenotype, and subjected to either Sanger sequencing (of the *his-72* gene) or DNA extraction and whole genome sequencing. To map the *ubc-20* suppressor, the suppressor strain was backcrossed to unmutagenized K27M mutants. F2s were clonally expanded and the causal suppressor mutation was followed by Western blotting for rescued H3K27me3. Library preparation and sequencing of genomic DNA was performed by BGI Genomics, using 150 bp paired-end reads. A depth of 20–35x coverage was obtained for all samples. In Galaxy, fastq files were aligned to the *ce10* genome using Bowtie2, and variants were called using MiModD. A genotype quality (>60) filter was applied, and variants present in both mutagenized and unmutagenized parental strains were filtered out.

Brood Size Assays. To determine brood sizes at 20 °C, two L4 animals were picked onto individual 6 cm plates seeded with OP50, and the number of live progeny was counted and averaged. To determine brood sizes at 25 °C, three L2–3 animals were picked onto individual 6 cm plates seeded with OP50, and the number of live progeny was counted and averaged.

RNAi. Animals were picked onto plates seeded with RNAi as L4s. For all RNAi except *mes-3*, animals were exposed to RNAi for two generations, and F2 L2s were collected for Western blot analysis. For *mes-3* RNAi, F1 L2s were collected due to the sterility of the F1 adults. For the E2 RNAi miniscreen (Fig. 3*I*), K27M mutants were crossed into an enhanced RNAi *(eri-1(mg366))* background to improve knockdown efficiencies. The empty L4440 vector was used as the control for all RNAi experiments.

Quantification of MES-2::GFP. Live animals were anesthetized in 1 mM levamisole in M9, mounted on 2% agarose pads, and placed under a microscope coverslip for imaging using a Nikon Ti microscope equipped with a 60× objective. Wide field fluorescence images were taken with a 12 ms exposure and mean GFP intensities in adult germline nuclei, and L2 larval pharyngeal nuclei were quantified in Fiji. At least 100 nuclei in 10 animals were assayed per condition per genotype.

Generation of Mutant Histone Constructs. cDNA sequences were synthesized by Twist Bioscience. Sequences consisted of full-length H3F3A cDNA containing desired mutations and a C-terminal FLAG-HA tag and were flanked by AttL1 and AttL2 sites to enable Gateway cloning into a custom CBioTAP IRES eGFP lentiviral vector. LR reactions were performed using 40 ng of the synthesized DNA fragment (equivalent to the "entry clone") and 150 ng of the destination vector, according to the manufacturer's protocol (Thermo Fisher 11791020). All cloned inserts were verified by Sanger sequencing.

Cell Culture. HEK293T cells were cultured in high glucose DMEM (Thermo Fisher) supplemented with 10% FBS (Gibco) and 1% Penicillin-Streptomycin. All cultures were grown at 37 °C and 5% CO_2, and checked every 2 mo for *Mycoplasma* contamination.

Lentivirus Production and Infection. HEK293T cells were seeded in 6-well plates at ~50% confluency one day prior to transfection. The following day, cells were transfected with 1.8 μg of histone expression construct, 1 μg of pMD2.G (Addgene 12259), and 1.2 μg of psPAX2 (Addgene 12260), with 6 μL of PEI. Viral supernatants were harvested 48 h posttransfection, 0.43 μm-filtered, and used for infections with 10 μg/ml polybrene.

Western Blotting. Animals were washed off plates in M9 + 0.05% Triton-X and pelleted by centrifugation. Live pellets (>30 μL) were resuspended in 4xLaemlli buffer containing 10% beta-mercaptoethanol in a total volume of >100 μL. Samples were frozen on dry ice and stored at −80 °C. Prior to Western blotting, samples were sonicated in a Bioruptor on high (30 s on, 30 s off for 2.5 mins), boiled at 95 to 100 °C for 5 min, and re-frozen at −80 °C. A second, identical round of sonication and boiling was then performed. Samples were spun down at 13,000 rpm for 10 mins and supernatant was loaded into SDS-PAGE gels. Separated proteins were transferred onto 0.2-μm nitrocellulose membranes and blocked in 5% milk for 1 h at room temperature. Primary antibodies (1:2,000 anti-H3K27me3, Cell Signaling Technology #9733; 1:1,000 anti-H3K27M, Abcam ab190631; 1:1,000 anti-H3K27me2, Cell Signaling Technology #9728; 1:1,000 anti-H3K36me2, Abcam ab9049; 1:10,000 anti-beta-Actin-HRP, Santa Cruz Biotechnology sc-47778 HRP; 1:2,000 anti-histone H4, Cell Signaling Technology #2592; 1:2,000 anti-histone H3, Cell Signaling Technology #9715; 1:1,000 anti-FLAG, Sigma-Aldrich F3165; 1:2,000 anti-GFP, Proteintech 50430-2-AP; 1:1,000 anti-H3K36me3, Abcam ab9050; 1:1,000 anti-Ubiquityl-Histone H2B (Lys120), Cell Signaling Technology #5546; 1:1,000 anti-Ubiquityl-Histone H2A(Lys119), Cell Signaling Technology #8240) were incubated overnight at 4 °C. The following day, membranes were washed 3x in PBST and nutated in 1:10,000 HRP-conjugated secondary antibody (Cell Signaling #7074 or #7076) for 1 h at room temperature. Signal was resolved using Clarity Western ECL Substrate (BioRad #1705061) and imaged on a BioRad Chemidoc.

Acid Extraction of Histones and Mass Spectrometry. First, ~500,000 starved L1 larvae were washed transferred from NGM plates into liquid culture for 3 d. Embryos were isolated from gravid adults by bleaching. Nuclei were isolated from embryos as previously described (68) and were lysed in nuclear lysis buffer (NLB) containing 420 mM NaCl, 50 mM Tris-HCl pH 7.4, 1.5 mM $MgCl_2$, 2 mM EDTA, 1 mM DTT, 20 mM sodium butyrate, with freshly added 1X protease inhibitor (Merck #11836170001), and phosphatase inhibitor (Merck #4906845001), by rocking at 4 °C for 5 mins. Samples were spun at 1,000 g for 5 mins to pellet insoluble material including histones, which were then released by adding 300 μL of NLB containing 2 M NaCl. H_2SO_4 was added to a final concentration of 0.2 M H_2SO_4 and samples were rocked overnight at 4 °C. Histones were precipitated in a final concentration of 25% TCA for 1 h on ice, washed twice in acetone, air-dried, and resuspended in 50 mM NH_4CO_3. Then, 10 to 20 μg of histones were obtained for each sample. Derivatization of histones was performed as described in Anastas et al. (35). In brief, histones were derivatized with a 1:3 mixture of propionic anhydride (Sigma Aldrich, Cat. # 240311):isopropanol (Sigma Aldrich, Cat. # 278475) followed by sample pH adjustment to pH ~8 with NH_4OH. The reaction was incubated at 37 °C for 15 mins, and sample volumes were reduced to ~5 μL by vacuum centrifugation before the next round of derivatization. Trypsin (Promega, V5111) digestion was performed for 6–8 h at 37 °C followed by two additional rounds of propionylation for a total of 4 derivatization steps. The resulting histone peptides

were analyzed by LCMS and relative label-free quantification was performed as described in Zee et al. (69).

Purification of pAG-Mnase. pAG-Mnase was purified from a 100 mL bacterial culture expressing Addgene (#123461). The bacterial pellet was resuspended in 15 mL of His buffer (50 mM Tris-HCl pH 7.4, 300 mM NaCl, 10 mM imidazole, and 0.5% NP-40, with freshly added PMSF to 1 mM). Further, 100 μL of 30 mg/ml lysozyme was added and the sample was incubated on ice for 30 mins, then sonicated with a Sonics Vibra-Cell Ultrasonic Processor, for 6 mins with settings: pulse 10 s on, 20 s off, at 25% amplitude. The lysate was spun at 4,000 rpm for 20 mins in a swinging bucket centrifuge to pellet debris. 750 μL of HisPur cobalt resin bead solution (Thermo Fisher #89965) was equilibrated in His buffer and added to 15 mL of the cleared lysate. The sample was rotated for 2 h at 4 °C, and washed 3x in His buffer. Elution was performed with 300 μL of elution buffer (850 μL His buffer + 150 μL of 1 M imidazole). The eluate was dialyzed twice against 500 mL dialysis buffer (10 mM Tris-HCl pH 7.4, 150 mM NaCl, 1 mM EDTA, 1 mM PMSF) to remove imidazole, with a Slide-a-Lyzer mini 7,000 MW (Thermo Fisher #69560). The concentration of the purified pAG-Mnase enzyme stock was measured by Bradford assay and diluted to 20 ng/μL with a final concentration of 50% glycerol. Then, ~2 mL of this enzyme stock was obtained from a 100 mL bacterial culture, and 1 μL (~20 ng pAG-Mnase) was used per 50 μL CUT&RUN reaction. Highly concordant H3K27me3 profiles in *C. elegans* embryos were obtained using in-house-purified vs. commercial pAG-Mnase (Cell Signaling Technology #86652).

CUT&RUN. *C. elegans* were grown to starvation on NA22-seeded plates at 20 °C. L2 larvae (starved for ~24 h) were washed off and dissociated into single cells according to refs. 70 and 71 with minor modifications. For each sample, ~30 μL of a live worm pellet was resuspended in 300 μL SDS-DTT solution (20 mM HEPES pH 7.4, 0.25% SDS, 200 mM DTT, 3% sucrose) for 4 mins at room temperature, then washed 3x in M9 buffer with 0.01% Triton, then 2x in egg buffer (25 mM HEPES pH 7.4, 118 mM NaCl, 48 mM KCl, 2 mM $CaCl_2$, 2 mM $MgCl_2$). Samples were digested in 200 μL of 15 mg/ml pronase (Merck 10165921001) for 25 mins at room temp, with repeated pipetting to obtain a single cell suspension. Digestion was stopped by adding 1 mL of DMEM + 10% FBS. Samples were then spun at 12 g (350 rpm) for 2 mins to pellet debris. The supernatant was collected and spun at 600 g for 3 mins to pellet cells, and following steps were performed according to standard CUT&RUN (72) with minor modifications. Cells were washed 2× in CUT&RUN wash buffer (20 mM HEPES pH 7.4, 0.5 mM spermidine, 150 mM NaCl, and 1 Roche EDTA-free protease inhibitor tablet per 50 mL buffer). Then, 10 μL of Concavalin A beads (Bangs Laboratories, BP531) was added to each sample and incubated at room temperature for 10 mins with periodic shaking. Beads were resuspended in 50 μL of antibody body binding buffer (CUT&RUN wash buffer + 0.05% digitonin + 2 mM EDTA) containing 1:100 primary antibody (anti-H3K27me3, Cell Signaling Technology #9733; anti-H3K27M, Abcam ab190631; IgG control, Cell Signaling Technology #66362) and nutated overnight at 4 °C. The next day, beads were washed once in Dig wash buffer (CUT&RUN wash buffer + 0.05% digitonin) and resuspended in 50 μL Dig wash buffer with 1 μL pAG-Mnase. Samples were nutated at 4 °C for 1 h, washed 2x in Dig wash buffer, and resuspended in 50 μL Dig wash buffer + 1 μL of 100 mM $CaCl_2$ to activate Mnase digestion for 30 mins on ice. Digestion was stopped by adding 2xSTOP buffer (340 mM NaCl, 20 mM EDTA, 4 mM EGTA, 0.05% digitonin, 30 μg/ml Rnase A, and 0.5 pg/μL of spike-in DNA from *S. cerevisiae* (Cell Signaling Technology). DNA was purified using Monarch PCR & DNA Cleanup columns (NEB T1030S) and quantified by Qubit. Libraries were prepared using NEB Ultra II DNA Library Prep Kit for Illumina (E7645L) according to the manufacturer's protocol and size selection was performed using Ampure XP beads (Beckman Coulter A63881). Then, 50 bp paired-end sequencing was performed on a Nextseq 2000. At least 10 million reads were obtained for each sample. Three replicate CUT&RUN reactions were performed per condition.

CUT&RUN Analysis. Reads were aligned to the *C. elegans ce11* (target genome) and *Saccharomyces cerevisiae sacCer3* (spike-in genome) using Bowtie2 v2.3.5.1, with settings --no-unal --local --very-sensitive-local --no-mixed --no-discordant --phred33 -I 10 -X 700. Bam files were sorted and indexed using samtools v1.8. Spike-in-normalized bigwig track files were created using bamCoverage from deepTools v3.3.1, with settings --binSize=20 --smoothLength=60 --normalizeUsing BPM --scaleFactor $scale_factor, where $scale_factor = the ratio of total reads/spike-in reads. Bigwig files from replicate experiments were averaged and merged for visualization using the bigWigMerge and bedGraphToBigWig commands from the UCSC Genome Browser's utilities.

For Fig. 4*A*, bedgraph files for individual replicates were generated using bamCoverage from deepTools v3.3.1, with settings --binSize = 5,000 --normalizeUsing BPM --scaleFactor $scale_factor, where $scale_factor = the ratio of total reads/spike-in reads. The H3K27me3 CUT&RUN signal within a given 5 kb window was averaged among triplicates. Regions with >500 spike-in normalized read counts in wild-type (n = 99, 0.4% of all 5 kb windows) were filtered out from all samples, and the H3K27me3 signal from the remaining 22,749 windows were plotted by their starting coordinate, divided by the total length of the chromosome, such that all chromosome lengths were normalized to 1.

Data, Materials, and Software Availability. Next generation sequencing data have been deposited in GEO (GSE275118) (73).

ACKNOWLEDGMENTS. We thank all members of the Shi lab for valuable discussion and feedback on the manuscript. We thank Ross Tomaino of the Taplin Mass Spectrometry Facility for assistance with histone proteomic experiments. We also thank Dongning Rao and Lucille King for assistance with the suppressor screen. Fig. 6*D* was created with BioRender. This work was supported by core funding from the Oxford branch of the Ludwig Institute for Cancer Research, by the NIH (MH096066), and by a Fellowship Grant from the ChadTough Defeat DIPG Foundation.

Author affiliations: [a]Ludwig Institute for Cancer Research, Nuffield Department of Medicine, University of Oxford, Oxford OX3 7DQ, United Kingdom; and [b]Division of Newborn Medicine and Epigenetics Program, Department of Medicine, Boston Children's Hospital, Boston, MA 02115

Author contributions: A.L.J. and Y.S. designed research; A.L.J., E.S., B.M.Z., and F.W. performed research; A.L.J. and B.M.Z. analyzed data; and A.L.J. and Y.S. wrote the paper.

Reviewers: C.L., Columbia University Irving Medical Center; and C.V.R., Stanford University School of Medicine.

Competing interest statement: Y.S. is a co-founder of K36 Therapeutics and Alternative Bio (ABio) Inc and a member of the Scientific Advisory Board of Alternative Bio (ABio) Inc, Epigenica AB and Epic Bio, Inc. Y.S. is also a board member of ABio Inc and Epigenica AB. Y.S. holds equity in Active Motif, K36 Therapeutics, Epic Bio, Inc, Alternative Bio, Inc and Epigenica AB.

1. A. Mackay *et al.*, Integrated molecular meta-analysis of 1,000 pediatric high-grade and diffuse intrinsic pontine glioma. *Cancer Cell* **32**, 520–537.e5 (2017).
2. D. Sturm *et al.*, Hotspot mutations in H3F3A and IDH1 define distinct epigenetic and biological subgroups of glioblastoma. *Cancer Cell* **22**, 425–437 (2012).
3. D. A. Khuong-Quang *et al.*, K27M mutation in histone H3.3 defines clinically and biologically distinct subgroups of pediatric diffuse intrinsic pontine gliomas. *Acta Neuropathol.* **124**, 439–447 (2012).
4. J. Schwartzentruber *et al.*, Driver mutations in histone H3.3 and chromatin remodelling genes in paediatric glioblastoma. *Nature* **482**, 226–231 (2012).
5. G. Wu *et al.*, Somatic histone H3 alterations in pediatric diffuse intrinsic pontine gliomas and non-brainstem glioblastomas. *Nat. Genet.* **44**, 251–253 (2012).
6. J. Stafford *et al.*, Multiple modes of PRC2 inhibition elicit global chromatin alterations in H3K27M pediatric glioma. *Sci. Adv.* **4**, 432781 (2018).
7. S. Nagaraja *et al.*, Histone variant and cell context determine H3K27M reprogramming of the enhancer landscape and oncogenic state. *Mol. Cell* **76**, 965–980.e12 (2019). 10.1016/j.molcel.2019.08.030.
8. A. S. Harutyunyan *et al.*, H3K27M induces defective chromatin spread of PRC2-mediated repressive H3K27me2/me3 and is essential for glioma tumorigenesis. *Nat. Commun.* **10**, 1262 (2019).
9. P. W. Lewis *et al.*, Inhibition of PRC2 activity by a gain-of-function H3 mutation found in pediatric glioblastoma. *Science (80-.)* **340**, 857–861 (2013).
10. G. L. Brien *et al.*, Simultaneous disruption of PRC2 and enhancer function underlies histone H3.3-K27M oncogenic activity in human hindbrain neural stem cells. *Nat. Genet.* **53**, 1221–1232 (2021).
11. L. Di Croce, K. Helin, Transcriptional regulation by Polycomb group proteins. *Nat. Struct. Mol. Biol.* **20**, 1147–1155 (2013).
12. S. U. Jain *et al.*, H3 K27M and EZHIP impede H3K27-methylation spreading by inhibiting allosterically stimulated PRC2. *Mol. Cell* **80**, 726–735.e7 (2020).
13. F. Mohammad *et al.*, EZH2 is a potential therapeutic target for H3K27M-mutant pediatric gliomas. *Nat. Med.* **23**, 483–492 (2017).
14. A. P. Bracken, N. Dietrich, D. Pasini, K. H. Hansen, K. Helin, Genome-wide mapping of polycomb target genes unravels their roles in cell fate transitions. *Genes Dev.* **20**, 1123–1136 (2006).

15. R. Margueron, D. Reinberg, The Polycomb complex PRC2 and its mark in life. *Nature* **469**, 343–349 (2011).
16. K. Funato, T. Major, P. W. Lewis, C. D. Allis, V. Tabar, Use of human embryonic stem cells to model pediatric gliomas with H3.3K27M histone mutation. *Science (80-.)* **346**, 1529–1533 (2014).
17. M. G. Filbin *et al.*, Developmental and oncogenic programs in H3K27M gliomas dissected by single-cell RNA-seq. *Science (80-.)* **360**, 331–335 (2018).
18. A. B. Silveira *et al.*, H3. 3 K27M depletion increases differentiation and extends latency of diffuse intrinsic pontine glioma growth in vivo. *Acta Neuropathol.* **137**, 637–655 (2019). 10.1007/s00401-019-01975-4.
19. S. Jessa *et al.*, Stalled developmental programs at the root of pediatric brain tumors. *Nat. Genet.* **51**, 1702–1713 (2019).
20. J. D. Larson *et al.*, Histone H3.3 K27M accelerates spontaneous brainstem glioma and drives restricted changes in bivalent gene expression. *Cancer Cell* **35**, 140–155.e7 (2019).
21. N. Justin *et al.*, Structural basis of oncogenic histone H3K27M inhibition of human polycomb repressive complex 2. *Nat. Commun.* **7**, 1–11 (2016).
22. H. M. Herz *et al.*, Histone H3 lysine-to-methionine mutants as a paradigm to study chromatin signaling. *Science (80-.)* **345**, 1065–1070 (2014).
23. S. Bender *et al.*, Reduced H3K27me3 and DNA hypomethylation are major drivers of gene expression in K27M mutant pediatric high-grade gliomas. *Cancer Cell* **24**, 660–672 (2013).
24. K. M. Chan *et al.*, The histone H3.3K27M mutation in pediatric glioma reprograms H3K27 methylation and gene expression. *Genes Dev.* **27**, 985–990 (2013).
25. X. Wang *et al.*, Targeting of polycomb repressive complex 2 to RNA by short repeats of consecutive guanines. *Mol. Cell* **65**, 1056–1067.e5 (2017).
26. J. Choi *et al.*, DNA binding by PHF1 prolongs PRC2 residence time on chromatin and thereby promotes H3K27 methylation. *Nat. Struct. Mol. Biol.* **24**, 1039–1047 (2017).
27. S. Poepsel, V. Kasinath, E. Nogales, Cryo-EM structures of PRC2 simultaneously engaged with two functionally distinct nucleosomes. *Nat. Struct. Mol. Biol.* **25**, 154–162 (2018).
28. A. Piunti *et al.*, Therapeutic targeting of polycomb and BET bromodomain proteins in diffuse intrinsic pontine gliomas. *Nat. Med.* **23**, 493–500 (2017).
29. S. U. Jain *et al.*, PFA ependymoma-associated protein EZHIP inhibits PRC2 activity through a H3 K27M-like mechanism. *Nat. Commun.* **10**, 2146 (2019).
30. X. Wang *et al.*, Regulation of histone methylation by automethylation of PRC2. *Genes Dev.* **33**, 1416–1427 (2019). https://doi.org/10.1101/gad.328849.119.et.
31. C. Lee *et al.*, Automethylation of PRC2 promotes H3K27 methylation and is impaired in H3K27M pediatric glioma. *Genes Dev.* **33**, 1428–1440 (2019). https://doi.org/10.1101/gad.328773.119.vation.
32. C. S. Grasso *et al.*, Functionally defined therapeutic targets in diffuse intrinsic pontine glioma. *Nat. Med.* **21**, 555–559 (2015).
33. S. Nagaraja *et al.*, Transcriptional dependencies in diffuse intrinsic pontine glioma. *Cancer Cell* **31**, 635–652.e6 (2017).
34. B. Krug *et al.*, Pervasive H3K27 acetylation leads to erv expression and a therapeutic vulnerability in H3K27M gliomas. *Cancer Cell* **35**, 782–797.e8 (2019).
35. J. N. Anastas *et al.*, Re-programing chromatin with a bifunctional LSD1/HDAC inhibitor induces therapeutic differentiation in DIPG. *Cancer Cell* **36**, 528–544.e10 (2019).
36. Z. Z. Brown *et al.*, Strategy for "Detoxification" of a cancer-derived histone mutant based on mapping its interaction with the methyltransferase PRC2. *J. Am. Chem. Soc.* **136**, 13498–13501 (2014).
37. J. Berlandi *et al.*, Identification of genes functionally involved in the detrimental effects of mutant histone H3.3–K27M in Drosophila melanogaster. *Neuro. Oncol.* **21**, 628–639 (2019).
38. K. Delaney, M. Strobino, J. M. Wenda, A. Pankowski, F. A. Steiner, H3.3K27M-induced chromatin changes drive ectopic replication through misregulation of the JNK pathway in C. elegans. *Nat. Commun.* **10**, 1–15 (2019).
39. E. E. Capowski, P. Martin, C. Garvin, S. Strome, Identification of grandchildless loci whose products are required for normal germ-line development in the nematode Caenorhabditis elegans. *Genetics* **129**, 1061–1072 (1991).
40. V. Kasinath *et al.*, JARID2 and AEBP2 regulate PRC2 in the presence of H2AK119ub1 and other histone modifications. *Science* **80-**, 371 (2021).
41. H. Endo *et al.*, Nucleosome surface containing nucleosomal DNA entry/exit site regulates H3–K36me3 via association with RNA polymerase II and Set2. *Genes to Cells* **17**, 65–81 (2012).
42. J. F. Sarthy *et al.*, Histone deposition pathways determine the chromatin landscapes of h3.1 and h3.3 k27m oncohistones. *Elife* **9**, 1–18 (2020).
43. K. Finogenova *et al.*, Structural basis for PRC2 decoding of active histone methylation marks H3K36me2/3. *Elife* **9**, 1–30 (2020).
44. T. Picart *et al.*, Characteristics of diffuse hemispheric gliomas, H3 G34-mutant in adults. *Neuro-Oncology Adv.* **3**, 1–12 (2021).
45. B. Snel, S. van den Heuvel, M. F. Seidl, Caenorhabditis elegans MES-3 is a highly divergent ortholog of the canonical PRC2 component SUZ12. *iScience* **25**, 104633 (2022).
46. E. T. Kipreos, Ubiquitin-mediated pathways in C. elegans. *WormBook* 1–24 (2005), 10.1895/wormbook.1.36.1.
47. L. B. Bender *et al.*, The MES-2/MES-3/MES-6 complex and regulation of histone H3 methylation in C. elegans. *Curr. Biol.* **14**, 1639–1643 (2004).
48. J. Dover *et al.*, Methylation of histone H3 by COMPASS requires ubiquitination of histone H2B by Rad6. *J. Biol. Chem.* **277**, 28368–28371 (2002).
49. Z. W. Sun, C. D. Allis, Ubiquitination of histone H2B regulates H3 methylation and gene silencing in yeast. *Nature* **418**, 104–108 (2002).
50. N. P. Blackledge, R. J. Klose, The molecular principles of gene regulation by Polycomb repressive complexes. *Nat. Rev. Mol. Cell Biol.* **22**, 815–833 (2021).
51. H. H. Ng, R. M. Xu, Y. Zhang, K. Struhl, Ubiquitination of histone H2B by Rad6 is required for efficient Dot1-mediated methylation of histone H3 lysine 79. *J. Biol. Chem.* **277**, 34655–34657 (2002).
52. M. D. Stewart, T. Ritterhoff, R. E. Klevit, P. S. Brzovic, E2 enzymes: More than just middle men. *Cell Res.* **26**, 423–440 (2016).
53. A. J. Middleton, C. L. Day, The molecular basis of lysine 48 ubiquitin chain synthesis by Ube2K. *Sci. Rep.* **5**, 1–14 (2015).
54. Z. Chen, C. M. Pickart, A 25-kilodalton ubiquitin carrier protein (E2) catalyzes multi-ubiquitin chain synthesis via lysine 48 of ubiquitin. *J. Biol. Chem.* **265**, 21835–21842 (1990).
55. F. Geng, W. P. Tansey, Polyubiquitylation of histone H2B. *Mol. Biol. Cell* **19**, 3616–3624 (2008).
56. G. Cecere, S. Hoersch, M. B. Jensen, S. Dixit, A. Grishok, The ZFP-1(AF10)/DOT-1 complex opposes H2B ubiquitination to reduce Pol II transcription. *Mol. Cell* **50**, 894–907 (2013).
57. A. Laugesen, J. W. Højfeldt, K. Helin, Molecular mechanisms directing PRC2 recruitment and H3K27 methylation. *Mol. Cell* **74**, 8–18 (2019).
58. P. L. Hsu *et al.*, Structural basis of H2B ubiquitination-dependent H3K4 methylation by COMPASS. *Mol. Cell* **76**, 712–723.e4 (2019).
59. T. Miller *et al.*, COMPASS: A complex of proteins associated with a trithorax-related SET domain protein. *Proc. Natl. Acad. Sci. U.S.A.* **98**, 12902–12907 (2001).
60. M. I. Valencia-Sánchez *et al.*, Structural basis of Dot1L stimulation by histone H2B Lysine 120 ubiquitination. *Mol. Cell* **74**, 1010–1019.e6 (2019).
61. N. Minsky *et al.*, Monoubiquitinated H2B is associated with the transcribed region of highly expressed genes in human cells. *Nat. Cell Biol.* **10**, 483–488 (2008).
62. S. Bilokapic, M. Halic, Nucleosome and ubiquitin position Set2 to methylate H3K36. *Nat. Commun.* **10**, 3795 (2019).
63. K. S. Jani *et al.*, Histone H3 tail binds a unique sensing pocket in EZH2 to activate the PRC2 methyltransferase. *Proc. Natl. Acad. Sci. U.S.A.* **116**, 201819029 (2019).
64. M. D. Shahbazian, K. Zhang, M. Grunstein, Histone H2B ubiquitylation controls processive methylation but not monomethylation by Dot1 and Set1. *Mol. Cell* **19**, 271–277 (2005).
65. E. Oh *et al.*, Gene expression and cell identity controlled by anaphase-promoting complex. *Nature* **579**, 136–140 (2020).
66. A. Fatima *et al.*, The ubiquitin-conjugating enzyme UBE2K determines neurogenic potential through histone H3 in human embryonic stem cells. *Commun. Biol.* **3**, 262 (2020).
67. J. A. Arribere *et al.*, Efficient marker-free recovery of custom genetic modifications with CRISPR/Cas9 in caenorhabditis elegans. *Genetics* **198**, 837–846 (2014).
68. F. A. Steiner, S. Henikoff, Holocentromeres are dispersed point centromeres localized at transcription factor hotspots. *eLife*. **3**, e02025 (2014). 10.7554/eLife.02025.
69. B. M. Zee, A. A. Alekseyenko, K. A. McElroy, M. I. Kuroda, Streamlined discovery of cross-linked chromatin complexes and associated histone modifications by mass spectrometry. *Proc. Natl. Acad. Sci. U.S.A.* **113**, 1784–1789 (2016).
70. S. Zhang, D. Banerjee, J. R. Kuhn, Isolation and culture of larval cells from C. elegans. *PLoS One* **6**, e19505 (2011).
71. J. Cao *et al.*, Comprehensive single-cell transcriptional profiling of a multicellular organism. *Science (80-.)* **357**, 661–667 (2017).
72. P. J. Skene, S. Henikoff, An efficient targeted nuclease strategy for high-resolution mapping of DNA binding sites. *Elife* **6**, 1–35 (2017).
73. A. L. Jiao *et al.*, Data from "An E2 ubiquitin conjugating enzyme links diubiquitinated H2B to H3K27M oncohistone function." Gene Expression Omnibus. https://www.ncbi.nlm.nih.gov/geo/query/acc.cgi?acc=GSE275118. Deposited 18 August 2024.